

Article

Intelligent Data Driven Ensemble Approaches for Bending Strength Prediction of Ultra-High Performance Concrete Beams

Kennedy Silewu^{1,*}, Charles Kahanji¹, Lenganji Simwanda² and Miroslav Sykora²¹ Department of Civil and Environmental Engineering, School of Engineering, University of Zambia, Lusaka 10101, Zambia² Department of Structural Reliability, Klokner Institute, Czech Technical University in Prague, 160 00 Prague 6, Czechia

* Correspondence: kennedysilewu@gmail.com

How To Cite: Silewu, K.; Kahanji, C.; Simwanda, L.; et al. Intelligent Data Driven Ensemble Approaches for Bending Strength Prediction of Ultra-High Performance Concrete Beams. *Bulletin of Computational Intelligence* 2025, 1(1), 31–52. <https://doi.org/10.53941/bci.2025.100003>

Received: 3 August 2025

Revised: 29 August 2025

Accepted: 3 September 2025

Published: 9 September 2025

Abstract: Existing code equations for predicting the bending capacity of ultra high performance fiber reinforced concrete (UHPFRC) beams often show large scatter, with coefficients of variation (CoV) exceeding 30 to 60 %, leading to both overly conservative and unconservative estimates. This study develops a novel and explainable machine learning (ML) framework for accurate bending capacity prediction, representing the first systematic benchmarking of advanced ensemble ML methods against international and national design codes. An updated database of 264 experimental UHPFRC beam tests was compiled from the literature and partitioned into training (70%), validation (15%), and testing (15%) subsets. Six ensemble algorithms were optimized using Bayesian hyperparameter tuning with 10 fold cross validation, namely Random Forest (RF), Gradient Boosting Machine (GBM), Light Gradient Boosting Machine (LightGBM), Adaptive Boosting (AdaBoost), Categorical Boosting (CatBoost), and Extreme Gradient Boosting (XGBoost). The best performing models, CatBoost and XGBoost, achieved excellent predictive accuracy on unseen test data ($R^2 \approx 0.96$ to 0.97 , $RMSE \approx 15$ to 18 kN·m, $CoV \approx 10\%$) with essentially no systematic bias. These results clearly outperform code equations ($R^2 \approx 0.60$ – 0.70 , $CoV \approx 28$ – 64% , and biases up to 40%). Interpretability analysis using Shapley Additive Explanations (SHAP) confirmed that effective depth and reinforcement ratio are the dominant predictors of bending strength, followed by steel yield strength and section properties, while UHPC compressive strength and fiber parameters had relatively minor influence within the dataset range. The novelty of this study lies in presenting an integrated and interpretable ML framework that not only achieves superior predictive performance but also provides mechanistic insight into UHPFRC beam behavior. The proposed approach offers a reliable data driven complement to current design codes and has potential for practical adoption in structural engineering design and code development.

Keywords: UHPFRC beams; bending capacity; explainable AI; machine learning; ensemble models

1. Introduction

Ultra high performance fiber reinforced concrete (UHPFRC) represents a significant advancement in cementitious materials, recognized for its superior mechanical properties, including exceptional compressive strength, ductility, and durability [1,2]. With a minimum compressive strength exceeding 150 MPa and tensile strength between 7 and 9 MPa, UHPFRC demonstrates remarkable resistance to harsh environmental conditions, such as freeze-thaw cycles, making it highly suitable for sustainable and resilient infrastructure [3–5]. Its applications span a wide range of structural elements, including building components, bridges, architectural features, repairs,



and rehabilitation of structures, as well as utility towers, offshore platforms, and hydraulic structures [6,7].

Despite these benefits, the adoption of UHPFRC on a larger scale has been hindered by the absence of comprehensive design codes and the limited understanding of its material properties [8]. Although some guidelines exist for estimating the bending capacity of UHPFRC, no universally accepted standard has been developed to date [9]. This lack of standardized design procedures presents a significant challenge for structural engineers, who require reliable predictions of the bending capacity of UHPFRC beams to ensure safe, economical, and code compliant design. Predicting bending capacity is especially critical because it governs ultimate limit states and emerges from coupled mechanisms including crack initiation and localization, tension softening, reinforcement yielding, and size effects [10,11]. Simplified stress block formulations struggle to represent these nonlinear fracture processes and the redistribution observed in three point and four point tests, particularly when bending interacts with shear or when sections and loading histories are complex [12,13]. In UHPC and UHPFRC, distinct fracture behavior and post cracking ductility further challenge closed form predictions [14,15]. These factors motivate data driven models that learn interactions among geometry, reinforcement, and material parameters directly from experiments; ensemble tree methods are well suited because they capture strong nonlinearity and interactions, are robust on moderate datasets, and can be paired with transparent explanations and repeatability checks [16–18].

To understand the behavior of UHPFRC in flexure, several experimental and numerical studies have been conducted in the recent past. For example, Kahanji et al. [6] demonstrated that increasing fiber content significantly enhances the bending capacity and energy absorption of UHPFRC beams, while highlighting that design codes such as Eurocode 2 underestimate bending strength compared to experimental results, necessitating updated standards. Chen and Wang [19] and Huang et al. [20] investigated the effects of varying longitudinal reinforcement ratios, finding that higher ratios improve bending capacity but may shift failure modes from ductile to brittle. Similarly, Yang et al. [21] emphasized the role of steel fiber content in enhancing energy absorption, ductility, and toughness, though with diminishing returns at fiber contents exceeding 1.5%. Displacement-controlled tests by El-Helou and Graybeal [22] offered practical insights into structural performance and failure mechanisms, emphasizing the importance of understanding these behaviors for safety and design optimization.

These studies collectively highlight the unique bending behavior of UHPFRC, wherein peak moments occur during localized cracking, contrasting with conventional concrete that often peaks prior to significant cracking. Research has proposed sectional analysis approaches for understanding bending behavior, considering linear strain distributions, strain limits, and reinforcement rupture. Accurate prediction models require detailed knowledge of UHPFRC's compression and tensile stress-strain characteristics, as these influence the maximum moment capacity, which depends on crack localization or compression crushing. Post-localization bending capacity is typically avoided due to risks associated with reinforcement rupture, necessitating further research to quantify the relationship between crack opening, reinforcement rupture strain, and development length [23,24]. Such advancements are critical for optimizing design methodologies and ensuring the structural efficiency of UHPFRC under flexural loading.

Despite significant progress in the experimental and numerical analysis of UHPFRC, existing studies are often specialized in identifying specific effects. This specialization limits their generalizability to applications beyond the tailored experimental setups. However, the extensive datasets generated from these prior studies offer a valuable opportunity for using data driven approaches. By employing machine learning (ML) models, it is possible to gain deeper insights into the bending behavior of UHPFRC beams, enabling broader applicability and predictive capabilities beyond traditional methodologies.

The use of ML in structural engineering has demonstrated significant advantages in handling complex, nonlinear relationships, uncovering hidden patterns, and achieving predictive accuracies that often surpass traditional methods, leading to safer and more efficient designs. Numerous studies have explored ML applications in predicting the mechanical properties of various types of concrete, including compressive strength, elastic modulus, and tensile strength. For instance, [25] and Fan et al. [26] applied ML to predict the compressive strength and optimize the mix design of UHPC composites, respectively. Diverse ML models were used across different concrete types, such as support vector machines (SVM), neural networks (ANN), random forests (RF), and gradient boosting (GB), achieving accuracies as high as 98% in term of coefficient of determination (R^2) [27–29]. A comprehensive evaluation by Ye et al. [30] employed ten ML algorithms to predict UHPC shear strength, underscoring the value of exploring diverse algorithms to optimize predictions for material properties. Additional recent studies further underline the promise of interpretable, data driven models for cementitious composites and structural elements [31,32].

However, when it comes to the bending capacity problem of UHPFRC, limited studies in the literature have focused on applying ML to predict the bending capacity of UHPFRC beams. For instance, Solhmirzaei et al. [33] employed support vector machine regression (SVMR) and multigene genetic programming (MGGP) for this purpose,

but the lack of model interpretability limited their practical application. While Ye et al. [30] achieved promising results for shear capacity prediction using various ML models—including ensemble methods like CatBoost—and enhanced interpretability through SHAP (Shapley Additive Explanations), similar efforts for bending capacity remain scarce. In the context of bending capacity, Qin et al. [34] demonstrated that an interpretable Extreme Gradient Boosting (XGBoost) model, optimized with the Whale Optimization Algorithm (WOA) and interpreted using SHAP, achieved superior performance and provided valuable insights into the key factors influencing the bending capacity of reinforced UHPC beams compared to traditional methods. Similarly, Qian et al. [35] used Support Vector Machine (SVM), Multi-Layer Perceptron (MLP), and Gradient Boosting (GB), incorporating SHAP for interpretability, but their focus on UHPC mix design parameters rather than bending design reduced its direct applicability. Concurrently, Ergen and Katlav [36] employed five ML models, including Support Vector Regression (SVR), XGBoost, MLP, Random Forest (RF), and Extremely Randomized Trees (ERT), using SHAP to interpret their results.

The emphasis on ensemble models in this study is motivated by several factors. Ensemble tree methods, such as bagging and boosting, are particularly suitable for UHPFRC bending data: they effectively capture strong nonlinearities and feature interactions, handle heterogeneous inputs without strict scaling assumptions, and remain robust on modest sample sizes compared to deep neural networks. Moreover, they provide reliable regularization through shrinkage, subsampling, and early stopping [37, 38]. Prior research also demonstrates that RF- and GBM-type models often outperform single learners on structural datasets while preserving interpretability through SHAP analysis. Despite these advantages, prior studies rarely (i) benchmark multiple advanced ensembles against international and national code equations on a unified and updated database, (ii) quantify uncertainty relative to codes, and (iii) provide model explanations that align with mechanics. To address this gap, the present work compiles an updated database of 264 UHPFRC beam tests, develops and optimizes six ensemble models (RF, GBM, LightGBM, AdaBoost, CatBoost, and XGBoost) using Bayesian search with cross validation, rigorously benchmarks them against design codes, and employs SHAP to provide both global and local interpretability. The contributions are fourfold: (1) an updated and harmonized database of UHPFRC flexural tests; (2) the first systematic uncertainty-aware benchmarking of six ensembles against multiple design code equations on bending capacity; (3) an explainable pipeline that quantifies feature effects (global and local SHAP) and cross-checks them against mechanics; and (4) a repeatability analysis using multiple seeds and error bars to demonstrate robustness. The overall objective is to develop an explainable ensemble ML framework for predicting UHPFRC beam bending capacity, trained on the updated database, optimized via Bayesian search with cross validation, quantitatively benchmarked against international and national code equations (including uncertainty metrics), and interpreted using SHAP to identify the dominant physical drivers and their interactions.

2. Description of Database

The dataset consisted of 264 instances of UHPFRC beams tested for bending failure, compiled from 54 different studies [19,21,26–79] as summarized in Table A1 in the Appendix A. The beam samples include various cross sectional shapes: Rectangular (R), T-shaped (T), and I-shaped (I), as depicted in Figure 1. These beams were subjected to two types of bending failure modes: balanced compression-tension failure (C) and localized tension failure (L), and were tested using either three point (3P) or four point (4P) bending setups.

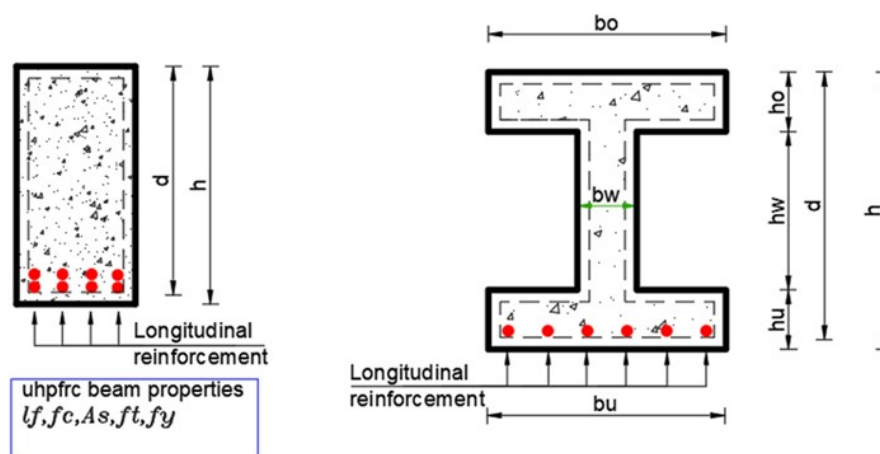


Figure 1. Section types in the database. Rectangular (**left**) and I-section (**right**).

Material properties of the UHPFRC beams encompass compressive strength (f_c), tensile strength (f_t), and yield strength of steel rebars (f_y). Additionally, the beams vary in reinforcement ratio (ρ_s), fiber aspect ratio (a_f), and fiber volume fraction (ρ_f). Geometric properties are denoted by beam width (b_o), web width (b_w), upper flange width (b_u), overall height (h), web height (h_o), web depth (h_w), upper flange height (h_u), and effective depth (d). For analytical purposes, the initial geometric parameters were reengineered to derive the concrete area (A_c) and the moment of inertia of the concrete section (I_c), which are critical in determining the moment capacity (M_c) of the beams. The refined dataset now features 10 input variables and 1 output variable, facilitating the training of supervised learning models.

Under the pre-processing stage of the data, all 264 observations were retained to preserve representativeness. Since tree-based ensembles are generally insensitive to feature scaling [80], no normalization is required. Instead, numeric features are winsorized at the 0.5th and 99.5th percentiles to reduce the influence of extreme values [81], and robust loss functions such as Huber or quantile regression are employed to further limit outlier effects during training [82].

The statistics for each parameter, outlined in Table 1, highlight the variability in the dataset, which ranges from fiberless UHPFRC to mixes with up to 3.8% fiber content, beam dimensions, and material strengths up to 216 MPa in compression and 57.7 MPa in tension. The dataset includes beams with reinforcement ratios as high as 11% and as low as 0%, offering a broad spectrum for analysis. Figure 2 presents histograms of the parameters, providing a visual summary of the data distribution and insights into the prevalent characteristics of the beams studied. These visualizations aid in understanding the underlying patterns and variations across the collected data.

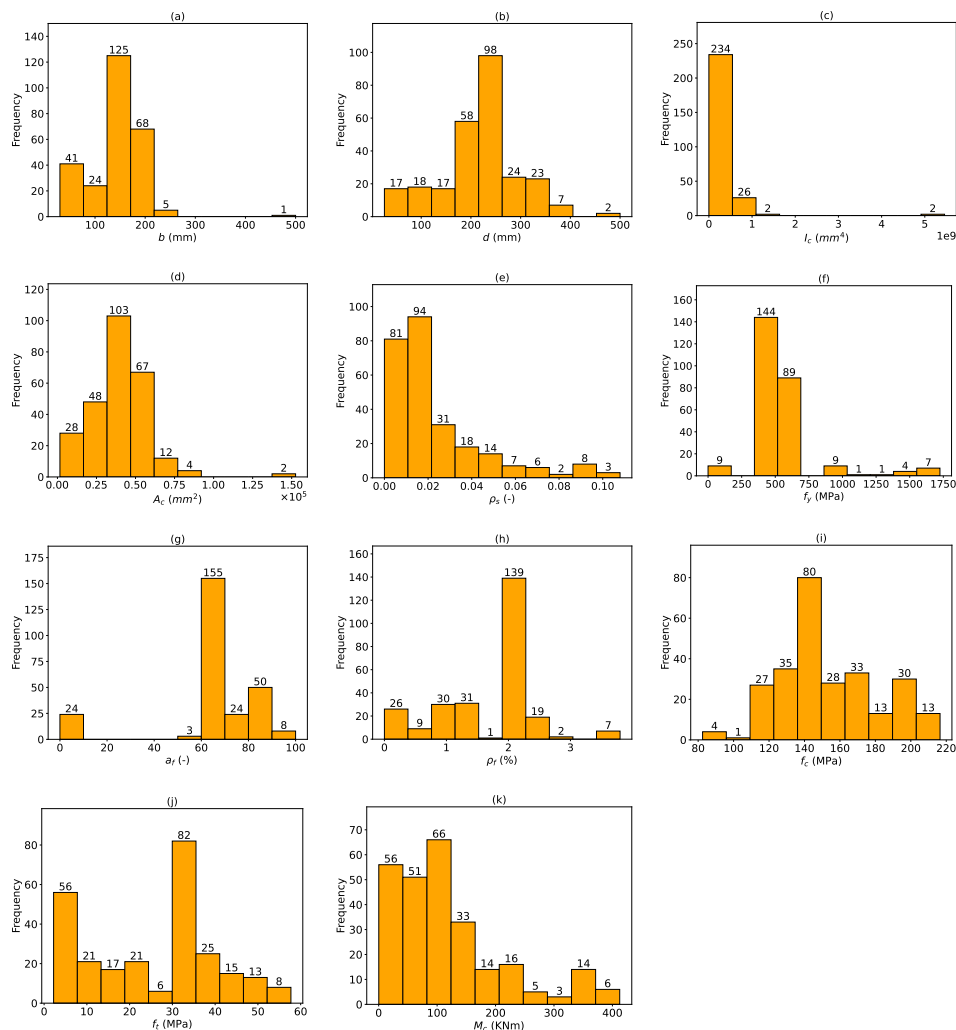


Figure 2. Statistical distribution of key parameters in the UHPFRC beam database, shown as histograms: (a) cross section width b , (b) effective depth d , (c) moment of inertia I_c , (d) cross sectional area of concrete A_c , (e) reinforcement ratio ρ_s , (f) steel yield strength f_y , (g) fiber aspect ratio a_f , (h) fiber volume fraction ρ_f , (i) compressive strength f_c , (j) tensile strength f_t , and (k) bending capacity M_c (experiment).

Table 1. Summary of statistical attributes of the database.

Parameter	Mean	Std	Min	Median	Max
b (mm)	143.7	51.5	30	150	500
d (mm)	216.3	82.1	26	220	500
I_c ($\times 10^6$ mm ⁴)	303.2	511.1	0.0	195.3	5457.3
A_c (mm ²)	39,440.9	19,488.5	1600	37,500	15,2500
ρ_s (-)	0.0275	0.0218	0.0042	0.00191	0.0873
f_y (MPa)	543.4	259.7	0.0	483.6	1725
a_f (mm)	64.0	22.1	0.0	65.0	100
ρ_f (%)	1.7	0.8	0.0	2.0	3.8
f_c (MPa)	154.0	27.2	82.5	146.0	216.5
f_t (MPa)	25.3	14.6	2.2	30.9	57.7
M_c (kN)	118.0	95.8	0.2	101.8	412.5

3. Correlation Analysis on Key Parameters

The bending capacity of UHPFRC members is primarily governed by three groups of parameters: the geometric dimensions and material properties of UHPFRC, as well as the geometric and material properties of longitudinal reinforcement, as detailed in Section 2. These parameters are commonly referred to as basic variables in design standards [83,84] or as input features in machine learning [37,38]. Within the scope of the collected database in this study, the steel fiber reinforcement ratio, ρ_f , ranges from 0 to 3.8%, encompassing both UHPC with and without fibers. This range highlights the influence of steel fibers on failure modes and tensile contributions to bending capacity. UHPFRC uniquely integrates the strengths of its material components—ultra high performance concrete, steel fibers, and steel rebars—maximizing their collective contribution to bending capacity. Consequently, the impact of steel fiber content on the bending capacity of UHPFRC beams is a focus of investigation. Various national design standards, including Chinese, Swiss, American, and French codes, provide methodologies for predicting the bending capacity of UHPFRC members. These approaches consistently emphasize the relationship between the basic variables and bending capacity. To facilitate comparison among these methods, Figure 3 illustrates the stress block geometries employed by each design model for singly reinforced UHPC beams under bending. The associated notations are detailed in the List of Symbols section.

(1) Method suggested by Draft Chinese UHPC code [85]

$$M_c = f_y A_s \left(d - \frac{a_c}{2} \right) + 0.5 f_t b_w a_t \left(h - \frac{a_c + a_t}{2} \right) \quad (1)$$

$$a_c = \frac{\beta_1 d}{1 + \frac{f_y}{E_s \varepsilon_{cu}}} \quad (2)$$

$$a_t = h - a_c / \beta_1 \quad (3)$$

$$\beta_1 = 0.88 - 0.005 f_c \quad (4)$$

(2) Method suggested by JGJ/T 465–2019 [86]

$$M_c = f_y A_s \left(d - \frac{a_c}{2} \right) + \beta_w V_f f_t b_w a_t \left(h - \frac{a_c + a_t}{2} \right) \quad (5)$$

(3) Method in Swiss SIA 2052 [87]

$$M_c = f_y A_s \left(d - \frac{c}{3} \right) + f_t b_w a_t (1.45h - 0.78c) \quad (6)$$

$$a_t = 0.9(h - c) \quad (7)$$

$$c = \frac{d}{1 + \frac{f_y}{E_s \varepsilon_{cu}}} \quad (8)$$

(4) Method in the American ACI 318 [88]

$$M_c = A_s \cdot f_y \cdot \left(d - \frac{a_c}{2} \right) \quad (9)$$

$$a_c = \frac{A_s \cdot f_y}{0.85 \cdot f_c \cdot b_w} \quad (10)$$

(5) Method in the American ACI 544 [89]

$$M_c = A_s f_y \left(d - \frac{a}{2} \right) + f_t b (h - e) \left(\frac{h + e - a}{2} \right) \quad (11)$$

$$c = \frac{A_s f_y + f_t b h}{f'_b \left(\frac{f_y + 0.003}{0.003} + 0.55 f'_c \right)} \quad (12)$$

$$e = \left(\frac{f_y + 0.003}{0.003} \right) c \quad (13)$$

$$a = 0.65c \quad (14)$$

$$\varepsilon_f = \frac{\sigma_{fs}}{E_{fs}} \quad (15)$$

$$\sigma_{fs} = 2\tau_s \left(\frac{l_f}{d_f} \right) \leq \sigma_{fy} \quad (16)$$

(6) Method in the American FHWA [90]

$$M_c = f_t b (h - c) \left(\frac{3h - c}{6} \right) + \rho_s f_y b h \left(d - \frac{c}{3} \right) \quad (17)$$

$$\rho_s = \frac{A_s}{b h} \quad (18)$$

$$c = \left(\frac{\rho_s f_y + f_t}{f_c + 0.5 f_t} \right) h \quad (19)$$

In existing models, the primary parameters influencing the bending capacity of UHPFRC members include the material strength of UHPFRC, the stress distribution in UHPFRC and steel, and the contributions from reinforcement. To simplify these models, certain assumptions are often made, such as the *plane section assumption* and the *equilibrium of internal forces*. Stress distributions are generally idealized as rectangular or triangular in both the compression and tension zones. However, these simplifications introduce limitations, as evidenced by scatter observed in comparative studies with experimental data, suggesting the models lack calibration for certain parameters [9,91].

To better understand the relationships between the bending capacity and various input parameters, a preliminary *Pearson correlation analysis* was conducted. The Pearson correlation coefficient r quantifies the linear relationship between two variables and is calculated as:

$$r = \frac{\sum_{i=1}^n (x_i - \bar{X})(y_i - \bar{Y})}{\sqrt{\sum_{i=1}^n (x_i - \bar{X})^2} \sqrt{\sum_{i=1}^n (y_i - \bar{Y})^2}} \quad (20)$$

where \bar{X} and \bar{Y} are the mean values of x_i and y_i , respectively.

The results of this analysis, as shown in Figure 4, indicate that geometric parameters, such as the moment of inertia (I_c), effective depth (d), longitudinal reinforcement ratio (ρ_s), and cross sectional area (A_c), exhibit stronger correlations with the bending strength (M_c) compared to material parameters, such as compressive strength (f_c), tensile strength (f_t), and steel fiber reinforcement ratio (ρ_f).

Figure 4 presents a Pearson correlation heatmap alongside a bar chart summarizing the correlation coefficients with M_c . The geometric parameters I_c ($r = 0.75$), d ($r = 0.62$), and A_c ($r = 0.66$) stand out as the most significant contributors to bending strength, while material parameters such as f_c ($r = 0.19$) and f_t ($r = -0.01$) show relatively weak correlations. This insight underscores the dominant role of geometric factors in influencing the bending capacity of UHPFRC members.

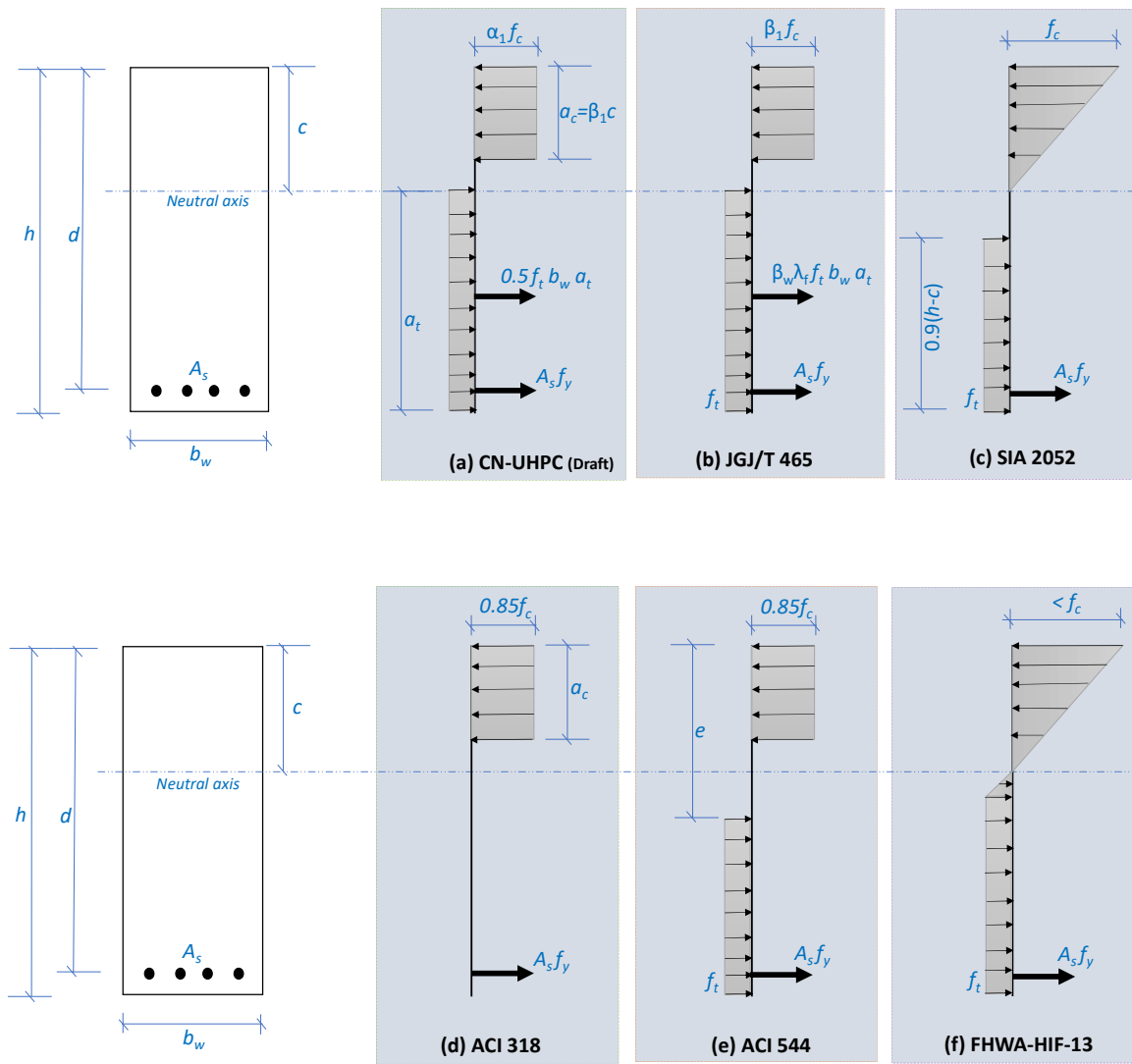


Figure 3. Stress block diagrams for bending capacity prediction models from different standards: (a) Draft Chinese UHPC code [70], (b) Chinese JGJ/T 465–2019 [71], (c) Swiss SIA 2052 [72], (d) ACI 318-19 [73], (e) ACI 544.4R-18 [74], (f) FHWA method [75].

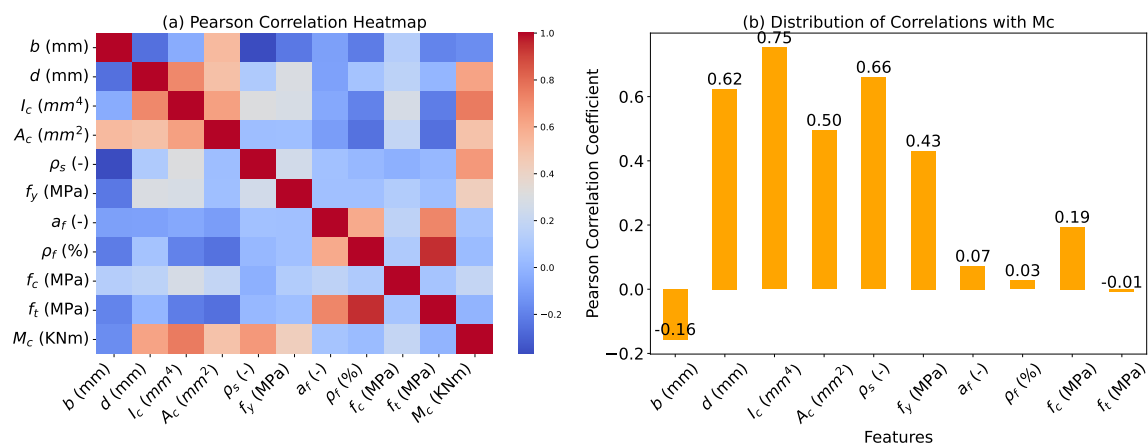


Figure 4. Pearson correlation coefficients of the input parameters with respect to the experimental bending capacity M_c . (Left: correlation heatmap; Right: bar chart of coefficient magnitudes $|r|$.) Geometric and reinforcement parameters (I_c , d , A_c , ρ_s , f_y) show the highest correlation with M_c , while material strength and fiber parameters (f_c , f_t , ρ_f , a_f) have relatively low correlation.

4. Development of Ensemble Models

4.1. ML Algorithms

This study employed six ensemble machine learning algorithms—RF, GBM, LightGBM, AdaBoost, CatBoost, and XGBoost—selected for their strong performance on nonlinear regression tasks common in engineering contexts [29, 92–94]. Only ensemble methods were considered; neural networks were not used. RF represents bagging: multiple decision trees are trained on bootstrap samples with feature subsampling and their predictions averaged, which reduces variance and improves stability under noisy conditions [37]. GBM represents boosting: shallow trees are added sequentially to fit the negative gradients of a chosen loss, thereby reducing bias but requiring regularization to avoid overfitting [37].

XGBoost should be understood as an advanced variant of GBM that integrates explicit regularization and systems-level optimizations: L_1/L_2 penalties on leaf weights, penalties on tree size, sparsity-aware split finding, approximate (weighted quantile) histograms, and parallelization, all of which improve generalization and training efficiency [38]. LightGBM further accelerates gradient boosting through histogram-based, leaf-wise tree growth (with depth limits) and data-reduction techniques such as Gradient-based One-Side Sampling (GOSS) and Exclusive Feature Bundling (EFB), delivering competitive accuracy with lower memory and time cost [37]. AdaBoost iteratively reweights observations to focus the learner on difficult cases, which can increase accuracy on hard regions but is controlled here via shallow base trees and early stopping [95]. CatBoost employs ordered boosting to mitigate prediction shift and reduce overfitting; although designed to handle categorical inputs efficiently, its ordered boosting and regularization also provide stability on purely numerical feature sets [37, 38]. Because tree splits are threshold-based, these ensemble methods are largely insensitive to feature scaling.

For model interpretability, SHAP [96] was used. Global SHAP values (dataset-level means of absolute attributions) were used to rank the overall influence of inputs on predicted bending capacity, while local SHAP values (instance-level attributions) explained individual predictions, enabling case-specific checks for physical plausibility. Figure 5 summarizes the end-to-end workflow (from preprocessing, to training/tuning, to evaluation, and to interpretation).

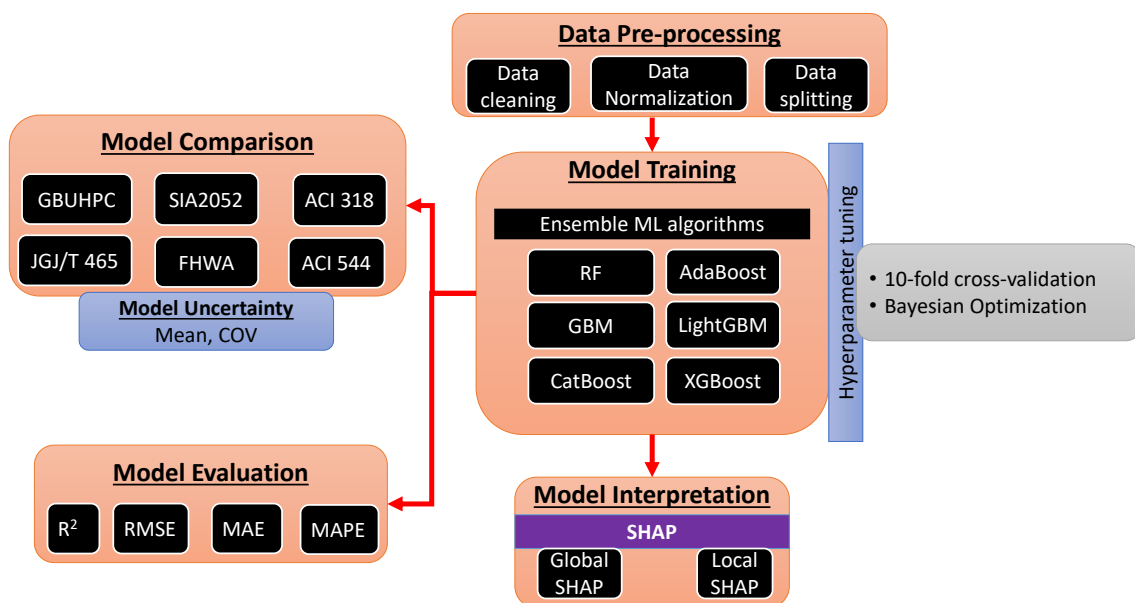


Figure 5. Workflow of the ensemble machine learning approach, illustrating the complete process from data preprocessing through model training, validation, and evaluation, to the development of design code equations and result interpretation.

4.2. Hyperparameter Tuning and Cross Validation

Hyperparameters, which are configurations set before training, are critical for optimizing model performance. This includes improving predictive accuracy, speeding up convergence, and minimizing overfitting. In this study, a 10-fold cross validation method was applied. The dataset was divided into 10 equal parts, with each part alternating as the validation set, while the others were used for training. This repetition over all ten folds ensures more reliable performance metrics and helps prevent overfitting. Instead of traditional grid search, Bayesian optimization via

Optuna was adopted for hyperparameter tuning. This method more efficiently searches the hyperparameter space by building a probabilistic model of the function mapping from hyperparameter values to the objective evaluated on a validation set. Previous studies have shown the efficient of this approach for hyperparameter tuning [97,98].

4.3. Model Training, Validation, and Evaluation

Models were trained on the UHPFRC dataset as detailed in Section 2. Following preprocessing, the dataset was split into 80% for training and 20% for testing [99]. During training, models learned to identify patterns and relationships between input features and the target variable, which is the bending capacity. To further alleviate overfitting, the training process incorporated 10-fold cross validation as previously mentioned. Four performance metrics were used to evaluate the models:

$$R^2 = 1 - \frac{\sum_{i=1}^n (y_i - \hat{y}_i)^2}{\sum_{i=1}^n (y_i - \bar{y})^2} \quad (21)$$

$$RMSE = \sqrt{\frac{1}{n} \sum_{i=1}^n (y_i - \hat{y}_i)^2} \quad (22)$$

$$MAE = \frac{1}{n} \sum_{i=1}^n |y_i - \hat{y}_i| \quad (23)$$

$$MAPE = \frac{100\%}{n} \sum_{i=1}^n \left| \frac{y_i - \hat{y}_i}{y_i} \right| \quad (24)$$

Here, y_i and \hat{y}_i are the actual and predicted values, \bar{y} is the mean value, and n is the number of samples. Higher R^2 values indicate better model fit, while lower RMSE, MAE, and MAPE values signify higher prediction accuracy.

5. Results and Discussion

5.1. Training and Testing Results

The performance of ensemble machine learning models, as measured by the performance metrics, is heavily influenced by the tuning of key hyperparameters. Using Bayesian optimization via Optuna [100], the optimal hyperparameters for the six models have been identified over a predefined range as shown in Table 2. Using these hyperparameters and the complete training dataset, six models were developed employing the respective ensemble methods. The performance of these models was evaluated on the testing dataset by comparing their predictions to the experimental data, as illustrated in Figure 6.

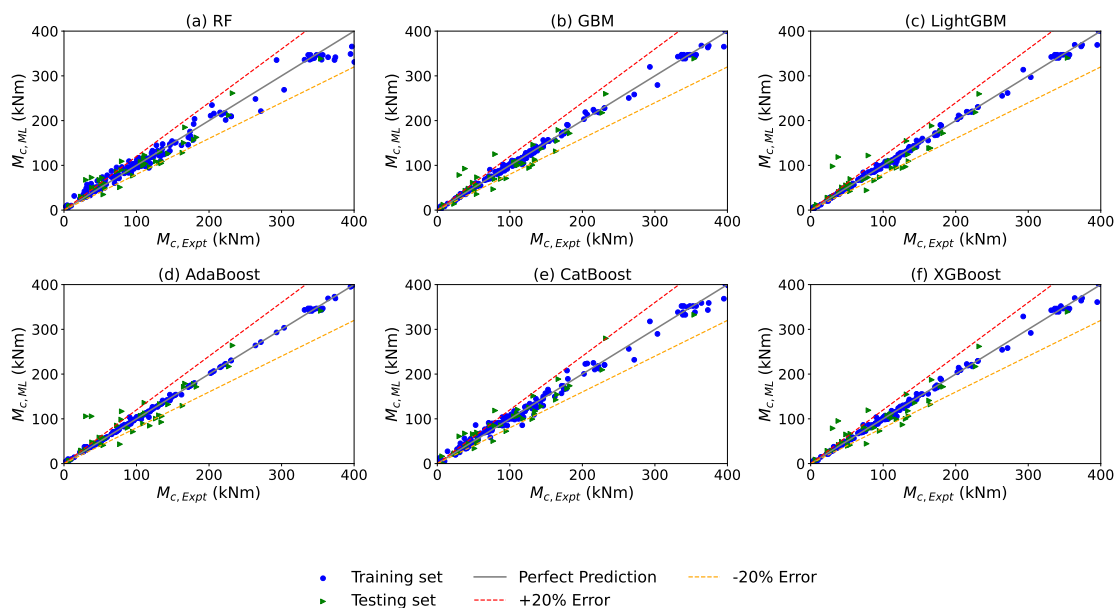


Figure 6. Predicted vs. experimental bending capacity for the ML models: RF, GBM, LightGBM, AdaBoost, CatBoost, and XGBoost. Results are shown for the training set (blue \circ) and testing set (green \triangle). The diagonal line represents perfect parity ($y = x$), and the dashed lines indicate $\pm 20\%$ error bands.

Table 2. Optimized hyperparameters found for RF, AdaBoost, GBM, LightGBM, CatBoost, and XGBoost after tuning.

ML Model	Hyper-Parameters	Domain	Optimal Value
RF	n_estimators	[100, 1000]	672
	max_depth	[10, 100]	26
	min_samples_split	[2, 20]	2
	min_samples_leaf	[1, 20]	1
	max_features	['sqrt', 'log2']	log2
	bootstrap	[True, False]	False
AdaBoost	n_estimators	[50, 1000]	950
	learning_rate	log-uniform [10 ⁻³ , 1.0]	0.12
	loss	['linear', 'square', 'exponential']	linear
	base_estimator	DecisionTreeRegressor (max_depth = [1, 10])	8
GBM	n_estimators	[100, 1000]	787
	max_depth	[3, 10]	3
	learning_rate	log-uniform [10 ⁻³ , 0.5]	0.07
	subsample	[0.5, 1.0]	0.53
	min_samples_split	[2, 20]	16
	min_samples_leaf	[1, 20]	2
	max_features	[0.5, 1.0]	0.83
	Test R ²	Fixed	0.91
LightGBM	n_estimators	[100, 1000]	197
	learning_rate	log-uniform [10 ⁻⁴ , 0.5]	0.07
	num_leaves	[10, 256]	73
	max_depth	[3, 15]	6
	min_child_samples	[5, 100]	15
	min_child_weight	log-uniform [10 ⁻³ , 10.0]	6.70
	subsample	[0.5, 1.0]	0.68
	colsample_bytree	[0.5, 1.0]	0.84
	reg_alpha	log-uniform [10 ⁻⁵ , 10.0]	3.95
	reg_lambda	log-uniform [10 ⁻⁵ , 10.0]	0.0006
CatBoost	iterations	[100, 1000]	596
	depth	[3, 10]	3
	learning_rate	log-uniform [10 ⁻³ , 0.5]	0.07
	l2_leaf_reg	log-uniform [10 ⁻³ , 10.0]	0.004
	bagging_temperature	[0.0, 1.0]	0.85
	random_strength	[10 ⁻⁵ , 10.0]	5.84
	border_count	[1, 255]	182
	loss_function	Fixed	RMSE
	verbose	Fixed	False
XGBoost	n_estimators	[100, 1000]	714
	max_depth	[10, 50]	42
	learning_rate	log-uniform [10 ⁻³ , 0.5]	0.18
	subsample	[0.5, 1.0]	0.58
	colsample_bytree	[0.5, 1.0]	0.53
	min_child_weight	[1, 10]	2
	reg_alpha	log-uniform [10 ⁻⁵ , 100.0]	2.49 × 10 ⁻⁵
	reg_lambda	log-uniform [10 ⁻⁵ , 100.0]	0.98
	objective	Fixed	reg:squarederror

The diagonal line ($y = x$) in Figure 6 indicates perfect agreement between the predicted and experimental values. Overall, all models' predictions align closely with the $y = x$ line with 89% of ML predictions falling within

$\pm 20\%$ of experimental values. This represents a significant improvement over the traditional code predictions with only 45–55% falling within $\pm 20\%$ band as discussed in Section 5.2. The small difference between training and testing performance for CatBoost suggests that its in-built regularization and robust features made it generalize well. In practice, the CatBoost model can predict UHPFRC beam capacity with a high degree of confidence across a range of input parameters, making it a promising tool for design assistance.

Furthermore, Figure 7 presents the performance measures (R^2 , RMSE, MAE, and MAPE) of the ensemble ML models on both the training and testing sets. To account for repeatability [101], each model was retrained ten times with different random seeds, and the mean \pm standard deviation of each metric is reported. The narrow error bars confirm that the models are stable and not sensitive to initialization or data partitioning. Among the models, CatBoost attained the highest accuracy, with $R^2 = 0.99 \pm 0.00$ on the training set and 0.94 ± 0.02 on the test set. XGBoost showed comparable performance ($R^2 = 0.94 \pm 0.02$ on test data), while RF achieved slightly lower but still strong generalization ($R^2 = 0.91 \pm 0.02$). The RMSE values for CatBoost and XGBoost on the test set were 23.6 ± 5.6 kN·m and 24.3 ± 4.6 kN·m, respectively, which are small relative to the experimental capacity range (up to 400 kN·m). The MAE for CatBoost was 15.4 ± 3.0 kN·m (about 5% of the average capacity), and its MAPE was $15.9 \pm 3.2\%$, highlighting low prediction error with tight variability. In contrast, LightGBM and AdaBoost exhibited higher test MAPEs ($\sim 20\text{--}24\%$), alongside larger train–test gaps, suggesting some degree of overfitting. Overall, the small standard deviations across metrics emphasize the repeatability and robustness of the ensemble models.

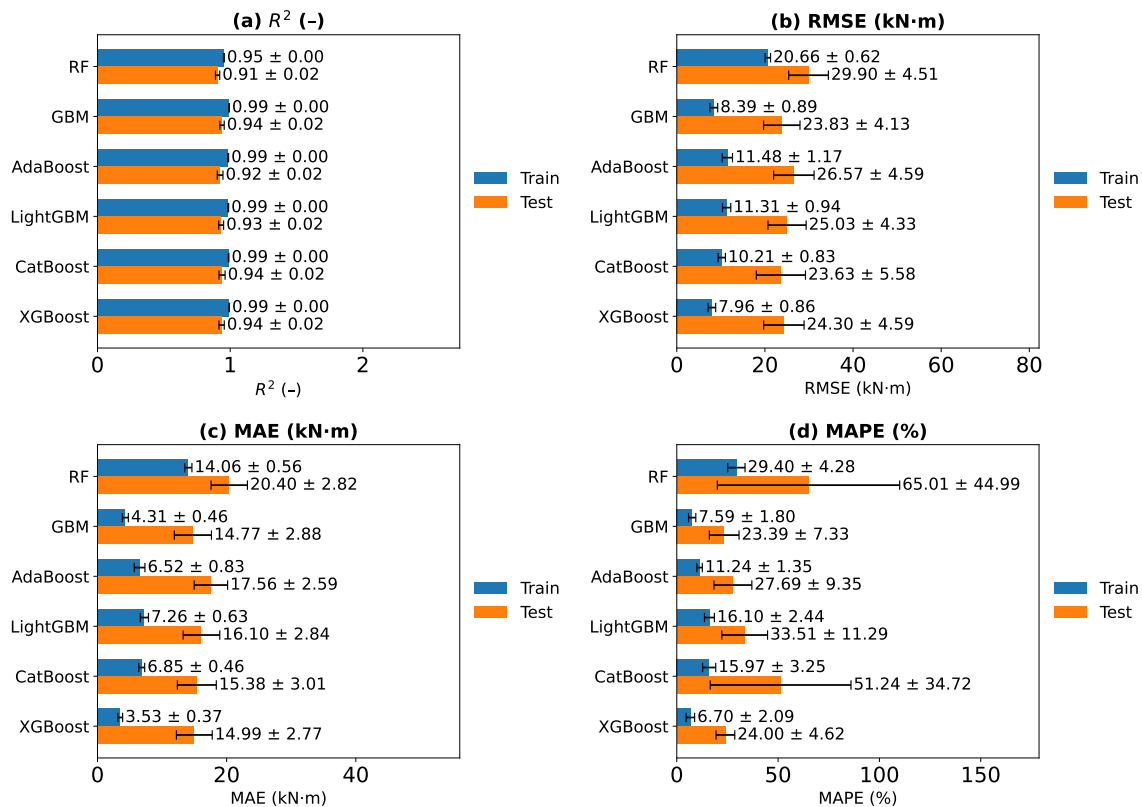


Figure 7. Performance of the six ensemble ML models on training and testing data: (a) R^2 , (b) RMSE, (c) MAE, and (d) MAPE. Bars show mean values across ten repeated runs with different random seeds, and error bars indicate the corresponding standard deviation, reflecting model repeatability and robustness. Blue bars represent training results and green bars represent test results.

5.2. Comparison Results with Analytical Models

We next compare the ML predictions with traditional analytical models from design codes. Figure 8 illustrates representative results: it shows the ratio of predicted-to-experimental capacity (M_{pred}/M_{exp}) for several code based methods and for the best performing ML model (CatBoost) across the entire dataset of 182 beams. Specifically, we investigate the following code models the Chinese draft method (denoted GBUHPC), the Chinese JGJ/T 465–2019 method, the Swiss SIA 2052 method, ACI 318, ACI 544, and the FHWA method. Table 3 provides a quantitative summary of the error statistics for each method, including the minimum, maximum, mean, and coefficient of variation (CoV) of the M_{pred}/M_{exp} ratio.

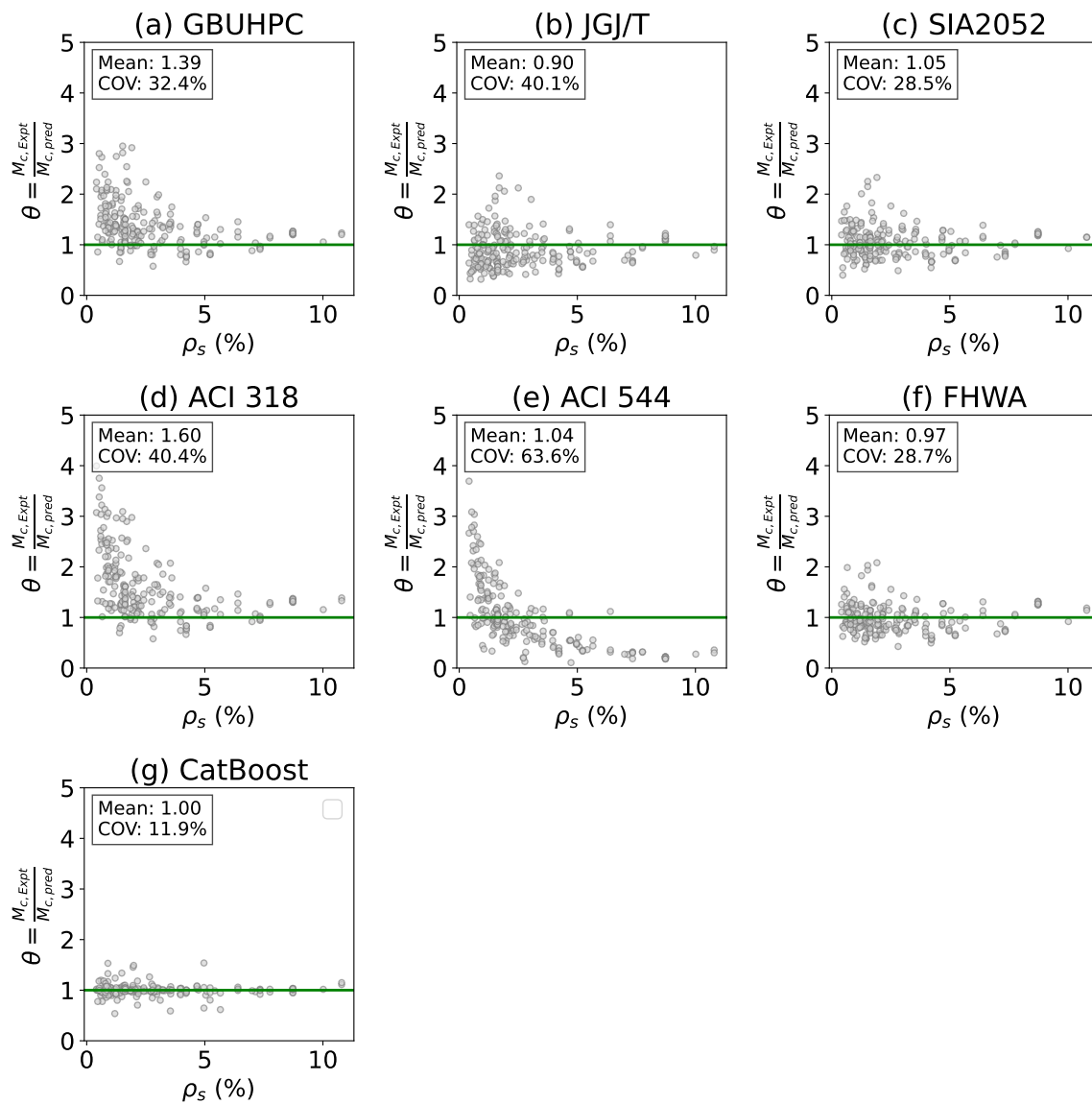


Figure 8. Comparison of analytical design equations and machine learning models (RF and XGBoost) against experimental results, shown as distributions of the predicted-to-experimental capacity ratio M_{pred}/M_{exp} . (a) Chinese draft UHPC code, (b) Chinese JGJ/T 465, (c) Swiss SIA 2052, (d) ACI 318-19, (e) ACI 544.4R-18, (f) FHWA method, and (g) CatBoost ML model. Each subplot indicates the mean and coefficient of variation (CoV) of the ratio for that method.

Table 3. Error statistics (prediction/experiment ratios) for various prediction methods.

Model	Minimum	Maximum	Mean	CoV (%)
CatBoost	0.54	1.54	1.00	11.87
FHWA	0.43	2.08	0.97	28.66
GBUHPC	0.58	2.95	1.39	32.36
SIA2052	0.40	2.33	1.05	28.53
JGJ465	0.32	2.36	0.90	40.09
ACI544	0.11	3.69	1.04	63.59
ACI318	0.58	3.99	1.60	40.45

The traditional code predictions exhibit significant scatter and bias. For instance, ACI 318 (which does not account for fiber contributions) grossly overestimates capacity on average (mean $M_{pred}/M_{exp} = 1.60$) with a CoV around 40%, meaning predictions are not only biased unsafe but also highly variable. ACI 544, which attempts to include fiber effects, has an almost unbiased mean (1.04) but an extremely high scatter (CoV $\approx 64\%$), indicating inconsistent accuracy. The Chinese draft method tends to over-predict capacity (mean 1.39, CoV 32%), whereas the

Chinese JGJ 465 method under-predicts on average (mean 0.90) and also shows large scatter (40% CoV). The Swiss SIA 2052 and FHWA methods fare slightly better, with means near 1.0 and CoVs around 28–29%, but still far less consistent than the ML models.

In stark contrast, the ML predictions by CatBoost are much more precise and accurate. CatBoost yields a mean ratio of 1.00 with CoV only 12%, essentially eliminating systematic bias and greatly reducing uncertainty. These results highlight that the data driven ML approach not only improves the average accuracy of bending capacity predictions but also significantly reduces the variability (uncertainty) compared to existing analytical models. In practical terms, an engineer using the CatBoost model could predict UHPFRC beam capacity with about $\pm 12\%$ typical variation, whereas using, say, the Chinese code might see $\pm 32\%$ or more variation and possible bias. Reducing this uncertainty can lead to more reliable and efficient designs (less need for overly conservative safety factors when the prediction is stable and unbiased).

5.3. Interpretation of ML Model Using SHAP Analysis

Understanding the influence of each input feature on the ML predictions is critical for interpreting the model behavior and building trust in these data driven approaches. We employed SHAP (Shapley Additive Explanations) to interpret the CatBoost model, which was the top-performing model in this study. SHAP provides a unified measure of feature importance by computing the contribution of each feature to the prediction for each data instance, based on cooperative game theory [96].

5.3.1. Feature Importance Analysis with Global SHAP

Figure 9 ranks the input features by their global importance, as measured by the mean absolute SHAP value for each feature. The features are sorted in descending order of their influence on the model's output. The reinforcement ratio (ρ_s) exhibits the highest importance (≈ 26.5), followed by the effective depth (d , ≈ 19.5). These two features clearly dominate the prediction of M_c , which aligns with correlation findings and engineering expectations—higher reinforcement content and greater beam depth significantly enhance bending capacity. The next most influential features are the steel yield strength (f_y , ≈ 18.5), the moment of inertia (I_c , ≈ 18.0), and the concrete area (A_c , ≈ 12.5), all of which reflect the cross sectional resistance to bending.

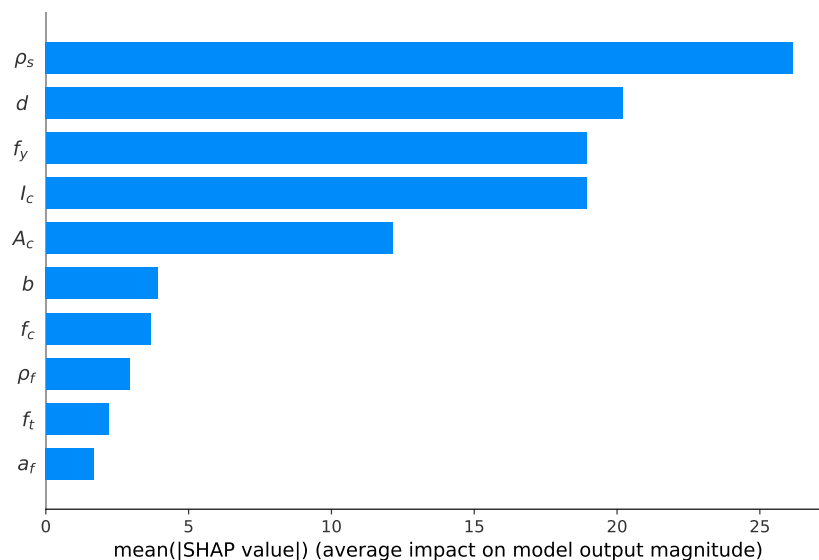


Figure 9. Global feature importance for the CatBoost model based on mean absolute SHAP values.

Geometric width b (≈ 4.0) has moderate importance. In contrast, the UHPC matrix compressive strength f_c (≈ 3.5) and the fiber-related parameters ρ_f (≈ 3.0), f_t (≈ 2.5), and a_f (≈ 2.0) contribute comparatively little. This suggests that, within the range of the dataset, fiber content and matrix strength variations have limited influence on bending capacity relative to geometry and reinforcement. This outcome is reasonable because most beams in the database use UHPC with f_c between 120–210 MPa and fiber content under 2%, so their effect is secondary compared with section size and steel reinforcement.

Figure 10 provides a SHAP summary plot (beeswarm plot) for the CatBoost model. Each point in this plot represents a SHAP value for one feature in one instance (beam) in the dataset, with color indicating the feature value

(red for high, blue for low). This plot offers additional insight into how each feature affects the prediction across its range. For example, in the d row (effective depth), red points (beams with larger d) are mostly on the right side (positive SHAP value), confirming that greater depth contributes positively to M_c . Conversely, for f_c , red points (higher concrete strength) are scattered around zero SHAP value, indicating no consistent effect—this supports the observation that increasing f_c within the given range does not significantly change the predicted capacity. The ρ_s row shows a clear trend where higher reinforcement ratios (red) correspond to positive SHAP contributions, while very low ρ_s (blue) have negative contributions, reinforcing the critical role of reinforcement amount.

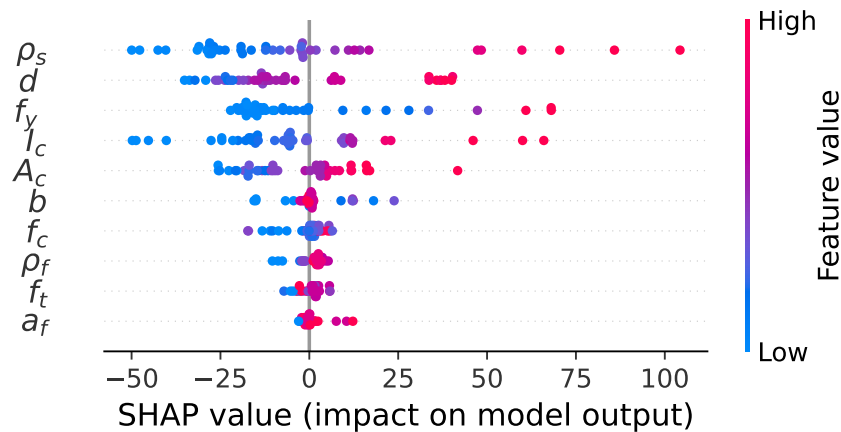


Figure 10. SHAP summary plot for the CatBoost model. Each point represents a feature’s SHAP value for one beam instance, with color indicating the feature’s actual value (red = high, blue = low). Features are ordered from most to least important on the vertical axis.

5.3.2. Feature Dependence Analysis with Local SHAP

While the global SHAP analysis above indicates overall importance, it is also useful to examine how changes in a single feature affect the predicted capacity, all else being equal. Figure 11 presents SHAP dependence plots for several key features (each subplot shows the SHAP value of a feature versus the feature’s actual value for all beams). These plots can be interpreted similarly to partial dependence plots, but they capture the actual model behavior including interaction effects.

From Figure 11a, we see that as the effective depth d increases (up to about 300 mm), the SHAP value is increasingly positive, meaning the model prediction of M_c rises significantly. Beyond roughly 300 mm, the SHAP contribution of further d increase tends to plateau or scatter, suggesting diminishing returns in that range (few beams had d much larger than 300 mm, so uncertainty increases). Figure 11b shows a strong positive dependence on ρ_s : increasing ρ_s from near 0 to about 0.05 (5%) yields a large increase in M_c contribution. There is a hint of saturation for $\rho_s > 0.05$ (the SHAP values level off), which may reflect yielding of steel or other limiting behaviors. Figure 11c indicates I_c (which grows with bh^3) has a generally positive effect—beams with larger I_c (due to larger section size) predictably have higher capacity, though the relationship is not perfectly linear due to correlations with other features (like d and b). Figure 11d for A_c similarly shows that larger cross sectional area contributes to higher M_c , mainly because it accompanies larger b or h . In contrast, Figure 11e for ρ_f (fiber content) is relatively flat: increasing fiber volume from 0% to about 2.5% yields only a small positive SHAP value on average. This aligns with our earlier observation that fiber contribution to ultimate moment is secondary (fibers mainly enhance post cracking ductility and shear; their direct addition to moment capacity in these tests was modest). A slight uptick at very high ρ_f (3.5%) can be seen, but our dataset had few such points. Figure 11f,g (not shown here for brevity) for f_y and f_c would indicate that higher steel yield strength clearly raises capacity (nearly linear relation in SHAP), whereas higher concrete compressive strength f_c does not appreciably change M_c in the model (SHAP values centered near zero across the range 120–210 MPa).

In summary, the SHAP analysis confirms that the ML model is capturing sensible structural behaviors: bending capacity increases with greater beam depth, width, and reinforcement, and is relatively insensitive to variations in UHPC matrix strength (within high-strength ranges) and fiber content as reported by various studies [6, 19, 24, 41]. This interpretability is important for engineering confidence, as it shows the model aligns with known mechanics (e.g., M_c is primarily governed by section modulus and reinforcement).

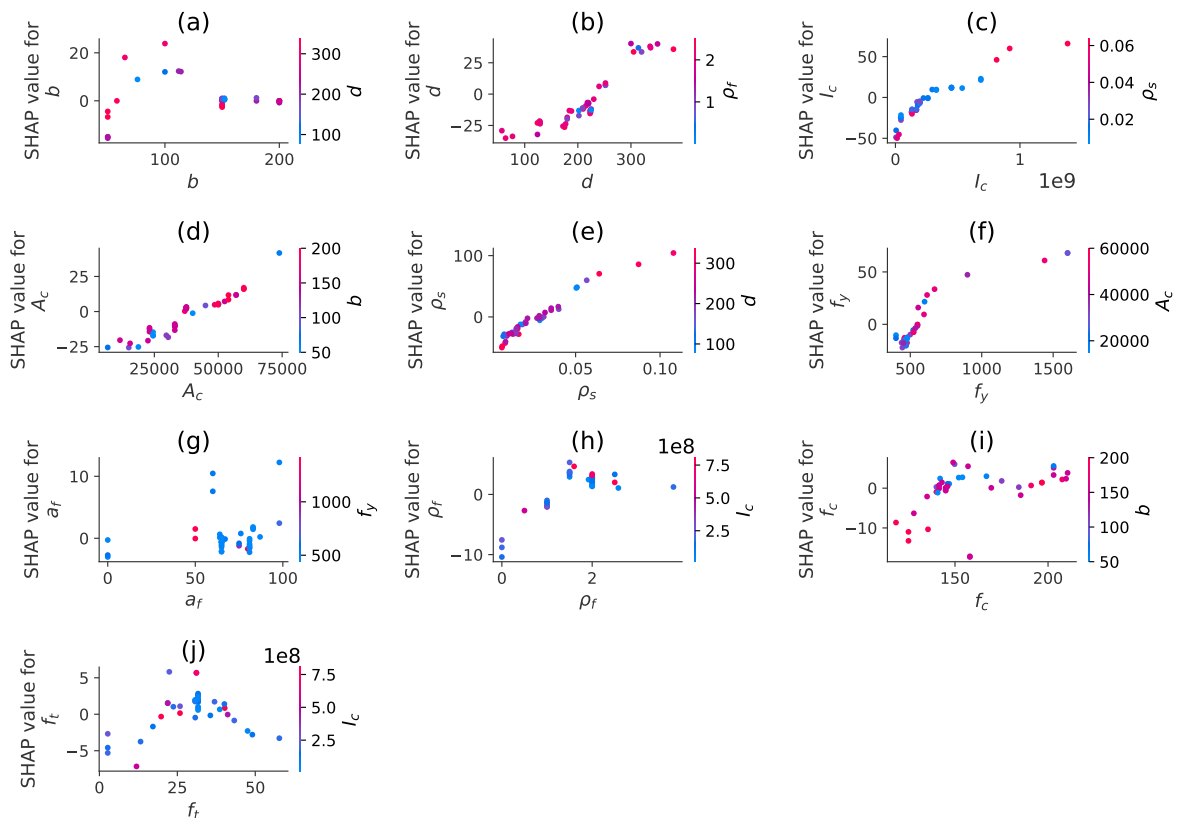


Figure 11. SHAP dependence plots for selected features: **(a)** b against d , **(b)** d against ρ_f , **(c)** I_c against ρ_s , **(d)** A_c against b , **(e)** ρ_s against d , **(f)** f_y against A_c , **(g)** a_f against f_y , **(h)** ρ_f against I_c , **(i)** f_c against b , and **(j)** f_t against I_c . Each point represents a beam; the vertical axis is the SHAP value (impact on predicted M_c) and the horizontal axis is the feature value.

5.4. Limitations

The dataset is modest in size and compiled across studies with heterogeneous protocols; true replicates under identical conditions are sparse. Feature coverage excludes certain determinants (e.g., detailed reinforcement layout, curing/age effects, fiber orientation), so extrapolation beyond the observed ranges is not supported. The models are purely data driven and do not enforce equilibrium/compatibility constraints; future work could integrate physics-informed regularization and expand the dataset to under-represented regimes.

6. Conclusions and Recommendations

This study developed and validated an intelligent, data driven framework for predicting the bending strength of ultra high performance fiber reinforced concrete (UHPFRC) beams using advanced ensemble machine learning algorithms. An updated database of 264 flexural tests compiled from 54 literature sources was used to benchmark six ensemble models (RF, GBM, LightGBM, AdaBoost, CatBoost, and XGBoost) against established international and national code equations. Hyperparameter optimization was performed via Bayesian search with 10-fold cross validation, and model repeatability was confirmed through multiple training runs with different random seeds.

The results demonstrate that ensemble ML models, particularly CatBoost and XGBoost, achieve state of the art predictive accuracy for beam bending capacity. CatBoost attained a mean R^2 of 0.99 ± 0.00 on the training set and 0.94 ± 0.02 on unseen test data, with a prediction-to-experiment ratio coefficient of variation (CoV) of only $\sim 12\%$. XGBoost showed comparable performance ($R^2 \approx 0.94 \pm 0.02$), while other models also delivered strong but slightly lower generalization. By contrast, conventional code based equations were significantly less reliable, with average R^2 values of only 0.60–0.70 and CoVs as high as 30–60%, underscoring the novelty and superiority of the data driven approach.

Beyond accuracy, the ML framework provides enhanced interpretability through SHAP analysis. Quantitative SHAP values revealed that reinforcement ratio (ρ_s , ~ 26.5) and effective depth (d , ~ 19.5) were the dominant drivers of bending capacity, followed by yield strength of steel and section properties. Material parameters such as compressive strength and fiber volume ratio had comparatively smaller effects within the tested ranges, highlighting

the model's ability to reflect physically meaningful mechanics. Importantly, the models captured complex multi-parameter interactions (e.g., between section geometry and reinforcement) that are difficult to represent in simplified design code formulas.

The proposed framework is novel in integrating (i) an updated and systematically compiled experimental database, (ii) rigorous ensemble model benchmarking, (iii) Bayesian optimization for robust hyperparameter tuning, and (iv) SHAP-based explainability. This combination delivers both predictive power and interpretability, positioning the approach as a reliable complement to existing design codes. In engineering practice, such models can be deployed to rapidly evaluate UHPFRC beam designs, perform sensitivity studies, and support reliability-based design.

Nonetheless, certain limitations must be acknowledged. The dataset, though extensive, remains modest in size and heterogeneous across experimental sources. Key variables such as reinforcement layout, curing conditions, and fiber orientation were not consistently reported, limiting the ability to generalize beyond the observed ranges. Moreover, the purely data driven models do not enforce equilibrium or compatibility conditions, and thus remain dependent on data quality and representativeness.

Future research should expand the updated database with new experiments covering under-represented beam geometries and higher fiber contents, integrate physics-informed constraints into ML frameworks, and extend the methodology to other structural behaviors such as shear strength and serviceability deflections. Ultimately, this study demonstrates that ensemble ML, when properly tuned and interpreted, provides a novel, accurate, and explainable pathway to improve prediction reliability for UHPFRC beams, offering valuable insights that can inform future analytical models and code provisions.

Author Contributions

K.S.: conceptualization, methodology, software; K.S.: data curation, writing—original draft preparation; K.S.: visualization, investigation; C.K.: supervision; L.S.: software, validation; M.S.: writing—reviewing and editing. All authors have read and agreed to the published version of the manuscript.

Funding

This research was funded by Czech Science Foundation under Grant24-10892S and Global Postdoctoral Fellowship Program of the Czech Technical University in Prague.

Institutional Review Board Statement

Not applicable.

Informed Consent Statement

Not applicable.

Data Availability Statement

All data, models, or scripts that support the findings of this study are available from the corresponding author upon reasonable request. The Python code and data that support the findings of this research are openly available on Mendeley Data (<https://data.mendeley.com/drafts/63g3fvhbz8>) and on Kaggle (<https://www.kaggle.com/code/lenganjjsimwanda/uhpc-flexure-ml/notebook>).

Acknowledgments

The involvement of Lenganji Simwanda in this research has been supported by the Global Postdoc Fellowship Program of the Czech Technical University in Prague, and the Czech Science Foundation under Grant 24-10892S.

Conflicts of Interest

The authors declare no conflict of interest.

Use of AI and AI-Assisted Technologies

During the preparation of this work, the authors used ChatGPT (OpenAI) to assist with language editing, structuring of technical content, and improving clarity and readability of the manuscript. After using this tool, the authors reviewed, verified, and edited all content as necessary and take full responsibility for the accuracy, originality, and integrity of the published article.

Notations

A_c	cross sectional area of concrete section
A_s	cross sectional area of reinforcement bars
a_c	Depth of the equivalent rectangular stress block
a_f	Aspect ratio of steel fibers
a_t	Height of the equivalent tensile stress block
b	Width of the beam cross section
b_o	Flange width of I-shaped and T-shaped UHPFRC beams
b_u	Top flange width of UHPFRC beam
b_w	Width of UHPFRC beam web
c	Neutral axis depth
d	Effective depth of the beam
d_f	Fiber diameter
e	Eccentricity of tensile force
E_s	Modulus of elasticity of steel
f_c	Compressive strength of UHPFRC
f_{tm}	Matrix (plain concrete) tensile strength of UHPFRC
f_t	Direct tensile strength of UHPFRC
f_y	Yield strength of reinforcement bars
f'_b	Adjusted compressive stress in beam (for composite stress block)
h	Overall section height of the beam
h_c	Height of UHPC flange for I-shaped/T-shaped beams
h_u	Height of UHPC top flange (T-shaped beams)
h_w	Web height of I-shaped/T-shaped beams
h_{vo}	Bottom flange height (T-shaped beams)
h_{vu}	Top flange height (T-shaped beams)
I_c	Moment of inertia of the concrete section
l_f	Fiber length
M_c	Ultimate bending moment capacity of the beam
V	Coefficient of variation
V_f	Fiber volume fraction (by volume)
β_1	Coefficient for equivalent compression zone height
β_w	Coefficient for steel fiber tensile contribution
μ	Mean value of a random variable
ρ_s	Longitudinal reinforcement ratio ($A_s/(bh)$)
σ_{fs}	Fiber tensile stress
τ_s	Shear strength contributed by fibers
θ	Model uncertainty factor
ϵ_{cu}	Ultimate compressive strain of concrete
ϵ_f	Tensile strain in fibers

Appendix A

A summary of the literature sources for the beam specimens in the dataset used for the ML implementation in this study is given in Table A1

Table A1. Summary of literature sources for UHPFRC beam tests (bending failure).

S/N	Reference	Year	No. of Beam Specimens	Failure Mode	Test Setup	C/S Shape
1	Bunje and Fehling [39]	2004	3	C	4P	R
2	Meade and Graybeal [7]	2010	10	L	3P	R
3	Yang et al. [21]	2010	10	L	4P	R
4	Stürwald [40]	2011	6	L	4P	R
5	Yang et al. [41]	2011	2	L	4P	I
6	Bertram and Hegger [42]	2012	1	C	3P	I
7	Randl et al. [43]	2013	8	C	4P	R

Table A1. Cont.

S/N	Reference	Year	No. of Beam Specimens	Failure Mode	Test Setup	C/S Shape
8	Hussein and Amleh [44]	2014	5	C	3P	R
9	Baby et al. [45]	2014	2	C	4P	I
10	Randl and Mészöly [46]	2014	8	C	4P	I
11	Yoo and Yoon [47]	2015	7	C	4P	R
12	Lim and Hong [48]	2016	2	C	3P	R
13	Li et al. [49]	2017	1	C	4P	R
14	Yoo et al. [50]	2017	5	L	4P	R
15	Pansuk et al. [51]	2017	3	C	3P	I
16	Chen and Wang [19]	2018	4	C	4P	R
17	Giesler et al. [52]	2018	2	L	4P	T
18	Hasgul et al. [53]	2018	8	C	4P	R
19	Kodur et al. [54]	2018	4	L	4P	R
20	Qi et al. [55]	2018	1	C	4P	R
21	Shafieifar et al. [56]	2018	4	C	3P	R
22	Yang et al. [57]	2018	7	C	4P	R
23	Gomaa and Alnaggar [58]	2019	5	C	3P	R
24	Pourbaba et al. [59]	2019	3	C	4P	R
25	Pourbaba et al. [60]	2019	5	C	4P	R
26	Shao and Billington [61]	2019	2	L	4P	R
27	Turker et al. [62]	2019	7	C	4P	R
28	Yavas et al. [63]	2019	1	C	4P	R
29	Hasgul et al. [64]	2019	3	L	4P	I
30	Liu et al. [65]	2019	5	C	4P	R
31	Qiu et al. [66]	2020	8	L	4P	R
32	Sturm et al. [67]	2020	2	L	3P	R
33	Yang et al. [68]	2020	10	C	4P	R
34	Qiu et al. [69]	2020	5	C	4P	T
35	Bae et al. [70]	2021	3	C	4P	R
36	Khan et al. [71]	2021	4	L	4P	R
37	Metje and Leutbecher [72]	2021	3	C	3P	R
38	Yavas and Ince [73]	2021	4	L	4P	I
39	Zhu et al. [74]	2021	4	C	4P	T
40	Bae and Choi [75]	2022	5	C	4P	R
41	Huß et al. [76]	2022	2	L	4P	R & I
42	Shao and Billington [77]	2022	4	L	4P	R
43	Sawicki et al. [78]	2022	7	L	4P	T
44	de Lima et al. [79]	2023	2	L	4P	R
45	Xiong et al. [102]	2023	12	L	4P	R
46	Liu et al. [103]	2023	2	L	4P	R
47	Guo and Wang [104]	2023	6	C	4P	R
48	Yan et al. [105]	2024	1	L	4P	R
49	Du et al. [106]	2025	3	L	4P	R
50	Tian et al. [107]	2024	5	L	4P	R
51	Wang et al. [108]	2025	10	C	3P	R
52	Yang et al. [109]	2023	10	C	3P	R
53	Jin et al. [110]	2025	4	C	3P	R
54	Ge et al. [111]	2023	13	C	4P	R

Note: C = Balanced compression-tension failure, L = Localised tension failure, 3P = Three-point bending test, 4P = Four-point bending test, R = Rectangular section, I = I-section, T = T-section.

References

1. Shafieifar, M.; Farzad, M.; Azizinamini, A. Experimental and numerical study on mechanical properties of ultra high performance concrete (uhpc). *Constr. Build. Mater.* **2017**, *156*, 402–411. <https://doi.org/10.1016/j.conbuildmat.2017.08.170>.
2. Simwanda, L.; Babafemi, A.J.; Koker, N.D.; et al. Bayesian calibration and reliability analysis of ultra high-performance fibre reinforced concrete beams exposed to fire. *Struct. Saf.* **2023**, *103*, 102352. <https://doi.org/10.1016/j.strusafe.2023.102352>.

3. Li, J.; Wu, Z.; Shi, C.; et al. Durability of ultra-high performance concrete—A review. *Constr. Build. Mater.* **2020**, *255*, 119296. <https://doi.org/10.1016/j.conbuildmat.2020.119296>.
4. Chu, H.; Zhang, Y.; Wang, F.; et al. Effect of graphene oxide on mechanical properties and durability of ultra-high-performance concrete prepared from recycled sand. *Nanomaterials* **2020**, *10*, 1718. <https://doi.org/10.3390/nano10091718>.
5. Wang, D.; Shi, C.; Wu, Z.; et al. A review on ultra high performance concrete: Part ii. hydration, microstructure and properties. *Constr. Build. Mater.* **2015**, *96*, 368–377. <https://doi.org/10.1016/j.conbuildmat.2015.08.095>.
6. Kahanji, C.; Ali, F.; Nadjai, A., Structural performance of ultra-high-performance fiber-reinforced concrete beams. *Struct. Concr.* **2017**, *18*, 249–258. <https://doi.org/10.1002/suco.201600006>.
7. Meade, T.M.; Graybeal, B.A. Flexural response of lightly reinforced ultra-high performance concrete beams. In Proceedings of the 3rd International fib Congress and Exhibition Incorporating the PCI Annual Convention and Bridge Conference: Think Globally, Build Locally, Washington, DC, USA, 29 May–2 June 2010.
8. Ullah, R.; Yuan, Q.; Ahmad, J.; et al. Ultra-high-performance concrete (uhpc): A state-of-the-art review. *Materials* **2022**, *15* 4131. <https://doi.org/10.3390/ma15124131>.
9. Feng, J.; Shao, X.; Qiu, M.; et al. Reliability evaluation of flexural capacity design provision for uhpc beams reinforced with steel rebars/prestressing tendons. *Eng. Struct.* **2024**, *300*, 117160. <https://doi.org/10.1016/j.engstruct.2023.117160>.
10. Carpinteri, A.; Corrado, M.; Mancini, G.; et al. Size-scale effects on plastic rotational capacity of reinforced concrete beams. *ACI Struct. J.* **2009**, *106*. <https://doi.org/10.14359/51663190>.
11. Carpinteri, A.; Corrado, M. Nonlinear fracture mechanics investigation on the ductility of reinforced concrete beams. *Rev. Ibracon Estruturas Mater.* **2010**, *3*, 137–148. <https://doi.org/10.1590/S1983-41952010000200002>.
12. Skarżyński, Ł.; Tejchman, J. Experimental investigations of fracture process using dic in plain and reinforced concrete beams under bending. *Strain* **2013**, *49*, 521–543. <https://doi.org/10.1111/str.12064>.
13. Recuperero, A.; Granata, M. Bending–shear interaction domains for externally prestressed concrete girders. *Adv. Civ. Eng.* **2013**, 1–13. <https://doi.org/10.1155/2013/580646>.
14. Zhurtov, A.; Khezhev, T.; Kokoev, M. An investigation of the stress-strain state of two-layer armoement structures on the power and temperature effects during a fire. *Mater. Sci. Forum* **2018**, *931*, 219–225. <https://doi.org/10.4028/www.scientific.net/MSF.931.219>.
15. Zhou, H.; Li, Z.; Guo, E.; et al. Test study on size effect of flexural capacity of rc cantilever beams. *Adv. Mater. Res.* **2012**, *446–449*, 3160–3164. <https://doi.org/10.4028/www.scientific.net/AMR.446-449.3160>.
16. Amin, M.N.; Iqbal, M.; Khan, K.; et al. Ensemble tree-based approach towards flexural strength prediction of frp reinforced concrete beams. *Polymers* **2022**, *14*, 1303. <https://doi.org/10.3390/polym14071303>.
17. Wang, X.; Ma, X.; Chen, S. Uncertainty-aware fuzzy knowledge embedding method for generalized structural performance prediction. *Comput.-Aided Civ. Infrastruct. Eng.* **2025**. <https://doi.org/10.1111/mice.13457>.
18. Waqas, H.; Bahrami, A.; Sahil, M.; et al. Performance prediction of hybrid bamboo-reinforced concrete beams using gene expression programming for sustainable construction. *Materials* **2023**, *16* 6788. <https://doi.org/10.3390/ma16206788>.
19. Chen, S.; Wang, J.Y. Flexural behaviour of rebar-reinforced ultra-high-performance concrete beams. *Mag. Concr. Res.* **2018**, *70*, 215–227. <https://doi.org/10.1680/jmacr.17.00283>.
20. Huang, J.; He, Z.; Khan, M.B.E.; et al. Flexural behaviour and evaluation of ultra-high-performance fibre reinforced concrete beams cured at room temperature. *Sci. Rep.* **2021**, *11*, 19069. <https://doi.org/10.1038/s41598-021-98502-x>.
21. Yang, I.H.; Joh, C.; Kim, B.S. Structural behavior of ultra high performance concrete beams subjected to bending. *Eng. Struct.* **2010**, *32*, 3478–3487. <https://doi.org/10.1016/j.engstruct.2010.07.017>.
22. El-Helou, R.; Graybeal, B. Flexural behavior and design of ultrahigh-performance concrete beams. *J. Struct. Eng.* **2022**, *148*, 04022013. [https://doi.org/10.1061/\(asce\)st.1943-541x.0003246](https://doi.org/10.1061/(asce)st.1943-541x.0003246).
23. Feng, Z.; Ke, L. Flexural and cracking behaviors of reinforced uhpc beams with various reinforcement ratios and fiber contents. *Eng. Struct.* **2021**, *245*, 113266. <https://doi.org/10.1016/j.engstruct.2021.113266>.
24. Fan, D.; Yu, R.; Shui, Z.; et al. A new design approach of steel fibre reinforced ultra-high performance concrete composites: Experiments and modeling. *Cem. Concr. Compos.* **2020**, *110*, 103597. <https://doi.org/10.1016/j.cemconcomp.2020.103597>.
25. Fan, D.; Yu, R.; Fu, S.; et al. Precise design and characteristics prediction of ultra-high performance concrete (uhpc) based on artificial intelligence techniques. *Cem. Concr. Compos.* **2021**, *122*, 104171.
26. Fan, D.; Zhu, J.; Fan, M.; et al. Intelligent design and manufacturing of ultra-high performance concrete (uhpc)—a review. *Constr. Build. Mater.* **2023**, *385* 131495.
27. Nguyen, H.; Vu, T.; Vo, T.; et al. Efficient machine learning models for prediction of concrete strengths. *Constr. Build. Mater.* **2021**, *266* 120950. <https://doi.org/10.1016/j.conbuildmat.2020.120950>.
28. Feng, D.; Wang, W.; Mangalathu, S.; et al. Implementing ensemble learning methods to predict the shear strength of rc deep beams with/without web reinforcements. *Eng. Struct.* **2021**, *235* 111979. <https://doi.org/10.1016/j.engstruct.2021.111979>.
29. Simwanda, L.; Sykora, M. Prediction of moment capacity of ultra-high-performance concrete beams using explainable extreme gradient boosting machine learning model. In Proceedings of the CEACM S4ML 2024 Conference, Prague, Czech Republic, 19–21 June 2024.

30. Ye, M.; Li, L.; Yoo, D.-Y.; et al. Prediction of shear strength in uhpc beams using machine learning-based models and shap interpretation. *Constr. Build. Mater.* **2023**, *408*, 133752. <https://doi.org/10.1016/j.conbuildmat.2023.133752>.
31. Mahmoud, A.A.; El-Sayed, A.A.; Aboraya, A.M.; et al. Synergizing machine learning and experimental analysis to predict post-heating compressive strength in waste concrete. *Struct. Concr.* **2025**, *26*, 2916–2950. <https://doi.org/10.1002/suco.202400211>.
32. Zeyad, A.M.; Mahmoud, A.A.; El-Sayed, A.A.; et al. Compressive strength of nano concrete materials under elevated temperatures using machine learning. *Sci. Rep.* **2024**, *14*, 24246. <https://doi.org/10.1038/s41598-024-73713-0>.
33. Solhmirzaei, R.; Salehi, H.; Kodur, V. Predicting flexural capacity of ultrahigh-performance concrete beams: Machine learning-based approach. *J. Struct. Eng.* **2022**, *148*, 1–13. [https://doi.org/10.1061/\(asce\)st.1943-541x.0003320](https://doi.org/10.1061/(asce)st.1943-541x.0003320).
34. Qin, S.; Li, J.; Song, R.; et al. Flexural capacity prediction of reinforced uhpc beams using an interpretable machine learning model. *Struct. Eng. Int.* **2024**, 1–12.
35. Qian, Y.; Sufian, M.; Hakamy, A.; et al. Application of machine learning algorithms to evaluate the influence of various parameters on the flexural strength of ultra-high-performance concrete. *Front. Mater.* **2023**, *9*, 1114510. <https://doi.org/10.3389/fmats.2022.1114510>.
36. Ergen, F.; Katlav, M. Machine and deep learning-based prediction of flexural moment capacity of ultra-high performance concrete beams with/out steel fiber. *Asian J. Civ. Eng.* **2024**, *25*, 4541–4562. <https://doi.org/10.1007/s42107-024-01064-2>.
37. Thai, H. Machine learning for structural engineering: A state-of-the-art review. *Structures* **2022**, *38*, 448–449.
38. Amezcua-Sanchez, J.; Valtierra-Rodriguez, M.; Adeli, H. Machine learning applications in structural engineering. *Stud. Syst. Decis. Control* **2024**, *547*, 47–76. <https://doi.org/10.1007/978-3-031-65976-83>.
39. Bunje, K.; Fehling, E., About shear force and punching shear resistance of structural elements of ultra high performance concrete. In Proceedings of the International Symposium on Ultra High Performance Concrete, Kassel, Germany, 13–15 September 2004; pp. 401–411.
40. Stürwald, S. *Versuche zum Biegetragverhalten von UHPC mit kombinierter Bewehrung*; Fachgebiet Massivbau, Fachbereich Bauingenieurwesen, Universität Kassel: Kassel, Germany, 2011.
41. Yang, I.H.; Joh, C.; Kim, B.S. Flexural strength of large-scale ultra high performance concrete prestressed t-beams. *Can. J. Civ. Eng.* **2011**, *38*, 1185–1195. <https://doi.org/10.1139/I11-078>.
42. Bertram, G.; Hegger, J. *Zum Verbund- und Querkrafttragverhalten von Spannbetonträgern aus Ultra-Hochfestem Beton*; Technical Report; Lehrstuhl und Institut für Massivbau, RWTH Aachen University: Aachen, Germany, 2012.
43. Randl, N.; Simon, C.; Mészöly, T. Experimental investigations on UHP(FR)C beams with high strength reinforcement. In Proceedings of the RILEM-fib-AFGC International Symposium on Ultra-High Performance Fibre-Reinforced Concrete (UHPFRC 2013), Marseille, France, 1–3 October 2013.
44. Hussein, L.; Amleh, L., Shear behavior of uhpfrc beams without stirrups, In Proceedings of the 10th fib International PhD Symposium in Civil Engineering, Laval, QC, Canada, 21–23 July 2014; pp. 437–442.
45. Baby, F.; Marchand, P.; Toutlemonde, F. Shear behavior of ultrahigh performance fiber-reinforced concrete beams. i: Experimental investigation. *J. Struct. Eng.* **2014**, *140*, 4013111. [https://doi.org/10.1061/\(ASCE\)ST.1943-541X.0000907](https://doi.org/10.1061/(ASCE)ST.1943-541X.0000907).
46. Randl, N.; Mészöly, T. The effect of fibres in UHPFRC beams with longitudinal steel reinforcement. In Proceedings of the Fibre-Reinforced Concrete: From Design to Structural Applications (FRC 2014: ACI-fib International Workshop Proceedings), Montreal, QC, Canada, 24–25 July 2014.
47. Yoo, D.Y.; Yoon, Y.S. Structural performance of ultra-high-performance concrete beams with different steel fibers. *Eng. Struct.* **2015**, *102*, 409–423.
48. Lim, T.; Hong, S. Shear tests for ultra-high performance fiber reinforced concrete (UHPFRC) beams with shear reinforcement. In Proceedings of the Fibre-Reinforced Concrete: From Design to Structural Applications (FRC 2014: ACI-fib International Workshop Proceedings), Montreal, QC, Canada, 24–25 July 2014.
49. Li, Y.; Guertin-Normoyle, C.; Algassem, O.; et al. Effect of ultra-high performance fibre reinforced concrete and high-strength steel on the flexural behaviour of reinforced concrete beams. In Proceedings of the AFGC-ACI-fib-RILEM Int. Symposium on Ultra-High Performance Fibre-Reinforced Concrete (UHPFRC 2017), Montpellier, France, 2–4 October 2017.
50. Yoo, D.Y.; Bantia, N.; Yoon, Y.S. Experimental and numerical study on flexural behavior of ultra-high-performance fiber-reinforced concrete beams with low reinforcement ratios. *Can. J. Civ. Eng.* **2017**, *44*, 18–28. <https://doi.org/10.1139/cjce-2015-0384>.
51. Pansuk, W.; Nguyen, T.N.; Sato, Y.; et al. Shear capacity of high performance fiber reinforced concrete i-beams. *Constr. Build. Mater.* **2017**, *157*, 182–193. <https://doi.org/10.1016/j.conbuildmat.2017.09.057>.
52. Giesler, A.J.; McGinnis, M.J.; Weldon, B.D. Flexural behavior and analysis of prestressed ultra-high-performance concrete beams made from locally available materials. *PCI J.* **2018**, *63*, 66–80. <https://doi.org/10.15554/pci63.6-02>.
53. Hasgul, U.; Turker, K.; Birol, T.; et al. Flexural behavior of ultra-high-performance fiber reinforced concrete beams with low and high reinforcement ratios. *Struct. Concr.* **2018**, *19*, 1577–1590. <https://doi.org/10.1002/suco.201700089>.
54. Kodur, V.; Solhmirzaei, R.; Agrawal, A.; et al. Analysis of flexural and shear resistance of ultra high performance fiber reinforced concrete beams without stirrups. *Eng. Struct.* **2018**, *174*, 873–884. <https://doi.org/10.1016/j.engstruct.2018.08.010>.
55. Qi, J.; Wang, J.; Ma, Z.J. Flexural response of high-strength steel-ultra-high-performance fiber reinforced concrete beams based on a mesoscale constitutive model: Experiment and theory. *Struct. Concr.* **2018**, *19*, 719–734. <https://doi.org/>

- 10.1002/suco.201700043.
56. Shafieifar, M.; Farzad, M.; Azizinamini, A. A comparison of existing analytical methods to predict the flexural capacity of ultra high performance concrete (uhpc) beams. *Constr. Build. Mater.* **2018**, *172*, 10–18. <https://doi.org/10.1016/j.conbuildmat.2018.03.229>.
 57. Yang, I.H.; Joh, C.; Kim, K.C. A comparative experimental study on the flexural behavior of high-strength fiber-reinforced concrete and high-strength concrete beams. *Adv. Mater. Sci. Eng.* **2018**, *2018*, 7390798. <https://doi.org/10.1155/2018/7390798>.
 58. Gomaa, S.; Alnaggar, M. Transitioning from shear to flexural failure of UHPC beams by varying fiber content. *Int. Interact. Symp. Ultra-High Perform. Concr.* **2019**, *2*, 9731. <https://doi.org/10.21838/uhpc.9731>.
 59. Pourbaba, M.; Sadaghian, H.; Mirmiran, A. Flexural response of uhpfrc beams reinforced with steel rebars. *Adv. Civ. Eng. Mater.* **2019**, *8*, 411–430. <https://doi.org/10.1520/ACEM20190129>.
 60. Pourbaba, M.; Sadaghian, H.; Mirmiran, A. A comparative study of flexural and shear behavior of ultra-high-performance fiber-reinforced concrete beams. *Adv. Struct. Eng.* **2019**, *22*, 1727–1738. <https://doi.org/10.1177/1369433218823848>.
 61. Shao, Y.; Billington, S.L. Utilizing full UHPC compressive strength in steel reinforced UHPC beams. In Proceedings of the 2nd International Interactive Symposium on Ultra-High Performance Concrete (2IIS-UHPC), Albany, NY, USA, 2–5 June 2019.
 62. Turker, K.; Hasgul, U.; Birol, T.; et al. Hybrid fiber use on flexural behavior of ultra high performance fiber reinforced concrete beams. *Compos. Part B Eng.* **2019**, *229*, 111400. <https://doi.org/10.1016/j.compstruct.2019.111400>.
 63. Yavas, A.; Hasgul, U.; Turker, K.; Birol, T. Effective fiber type investigation on the shear behavior of ultrahigh-performance fiber-reinforced concrete beams. *Adv. Struct. Eng.* **2019**, *22*, 1591–1605.
 64. Hasgul, U.; Yavas, A.; Birol, T.; Turker, K. Steel Fiber Use as Shear Reinforcement on I-Shaped UHP-FRC Beams. *Appl. Sci.* **2019**, *9*, 5526.
 65. Liu, C.; Zhang, Y.; Yao, Y.; Huang, Y. Calculation method for flexural capacity of high strain-hardening ultra-high performance concrete T-beams. *Struct. Concr.* **2019**, *20*, 405–419.
 66. Qiu, M.; Shao, X.; Zhu, Y.; Zhan, J.; Yan, B.; Wang, Y. Experimental investigation on flexural cracking behavior of ultrahigh performance concrete beams. *Struct. Concr.* **2020**, *21*, 2134–2153.
 67. Sturm, A.B.; Visintin, P.; Oehlers, D.J. Blending fibres to enhance the flexural properties of UHPFRC beams. *Constr. Build. Mater.* **2020**, *244*, 118328.
 68. Yang, I.H.; Park, J.; Bui, T.Q.; et al. An Experimental Study on the Ductility and Flexural Toughness of Ultrahigh-Performance Concrete Beams Subjected to Bending. *Materials* **2020**, *13*, 2225.
 69. Qiu, M.; Shao, X.; Wille, K.; Yan, B.; Wu, J. Experimental Investigation on Flexural Behavior of Reinforced Ultra High Performance Concrete Low-Profile T-Beams. *Int. J. Concr. Struct. Mater.* **2020**, *14*, 5.
 70. Bae, B.I.; Lee, M.S.; Choi, C.S.; Jung, H.S.; Choi, H.K. Evaluation of the ultimate strength of the ultra-high-performance fiber-reinforced concrete beams. *Appl. Sci.* **2021**, *11*, 2951.
 71. Khan, M.I.; Fares, G.; Abbas, Y.M.; et al. Behavior of non-shear-strengthened uhpc beams under flexural loading: Influence of reinforcement percentage. *Appl. Sci.* **2021**, *11*, 11168.
 72. Metje, K.; Leutbecher, T. Experimental investigations on the shear bearing behavior of prestressed ultra-high performance fiber-reinforced concrete beams with compact cross-section. *Struct. Concr.* **2021**, *22*, 3746–3762.
 73. Yavas, A.; Ince, M. Effect of reinforcement ratio on flexural behavior of I-shaped UHPFRC beams. *Structures* **2021**, *34*, 4457–4465.
 74. Zhu, L.; Li, T.; Wang, Y.; et al. Experimental and numerical study on T-Shaped UHPFRC beams with high-strength reinforcement. *Struct. Concr.* **2021**, *22*, 3630–3645.
 75. Bae, B.I.; Choi, H.K. Experimental Study on the Flexural Behavior of Lap-Spliced Ultra-High-Performance Fiber-Reinforced Concrete Beams. *Polymers* **2022**, *14*, 2138.
 76. Huß, M.; Waldenhofer, R.; Freytag, B.; et al. Zusammenwirken von Faser-und Betonstahlbewehrung bei biegebeanspruchten UHPC-Bauteilen. *Beton Stahlbetonbau* **2022**, *117*, 699–710.
 77. Shao, Y.; Billington, S.L. Impact of UHPC Tensile Behavior on Steel Reinforced UHPC Flexural Behavior. *J. Struct. Eng.* **2022**, *148*, 04021244.
 78. Sawicki, B.; Brühwiler, E.; Denarié, E. Inverse Analysis of R-UHPFRC Beams to Determine the Flexural Response under Service Loading and at Ultimate Resistance. *J. Struct. Eng.* **2022**, *148*, 04021260.
 79. de Lima, P.B.; Krahl, P.A.; Silva, F.A.; et al. A modeling strategy for the flexural performance prediction of UHPC beams accounting for variability of properties. *Compos. Struct.* **2023**, *322*, 117374.
 80. Breiman, L.; Friedman, J.; Olshen, R.; et al. *Classification and Regression Trees*; Wadsworth International Group: Belmont, CA, USA, 1984.
 81. Iglewicz, B.; Hoaglin, D. *How to Detect and Handle Outliers*; ASQC Quality Press: Milwaukee, WI, USA, 1993.
 82. Huber, P. Robust Estimation of a Location Parameter. *Ann. Math. Stat.* **1964**, *35*, 73–101.
 83. *EN 1990:2002*; Eurocode 0: Basis of Structural Design. European Committee for Standardization (CEN): Brussels, Belgium, 2002.

84. *CEN/TC 250/SC 2*; Background Document to FprEN 1992-1-1:2023—Eurocode 2: Design of Concrete Structures, Part 1-1: General Rules and Rules for Buildings, Bridges and Civil Engineering Structures. European Committee for Standardization (CEN): Brussels, Belgium, 2023.
85. Feng, J.; Shao, X.; Qiu, M.; et al. Reliability evaluation of flexural capacity design provision for UHPC beams reinforced with steel rebars/prestressing tendons. *Eng. Struct.* **2024**, *300*, 117160. <https://doi.org/10.1016/j.engstruct.2023.117160>.
86. *Chinese Standard JGJ/T 465-2019: Standard for Design of Steel Fiber Reinforced Concrete Structures*; Ministry of Housing and Urban-Rural Development of the People's Republic of China: Beijing, China, 2019.
87. *Swiss Standard (SIA 2052); MCS-EPFL Recommendation: Ultra-High Performance Fibre Reinforced Cement-Based Composites (UHPFRC)—Construction Material, Dimensioning and Application*. Swiss Society of Engineers and Architects (SIA): Zürich, Switzerland, 2016.
88. American Concrete Institute. *Building Code Requirements for Structural Concrete and Commentary*; ACI 318-19; American Concrete Institute: Indianapolis, ID, USA, 2019.
89. ACI Committee 544. *Design Considerations for Steel Fiber Reinforced Concrete*; Guide to Design with Fiber-Reinforced Concrete (Technical Report); American Concrete Institute: Farmington Hills, MI, USA, 2018.
90. Aaleti, S.; Petersen, B.; Sritharan, S. *Design Guide for Precast UHPC Waffle Deck Panel System, Including Connections*; Final Report; Federal Highway Administration, U.S. Department of Transportation: Washington, DC, USA; 2013.
91. Simwanda, L.; De Koker, N.; Viljoen, C. Structural reliability of ultra high-performance fibre reinforced concrete beams in flexure. *Eng. Struct.* **2021**, *244*, 112767.
92. Ye, M.; Li, L.; Jin, W.; et al. Interpretable ensemble machine learning models for predicting the shear capacity of UHPC joints. *Eng. Struct.* **2024**, *315*, 118443.
93. Madirisha, M.M.; Simw, A.L.; Mtei, R.P. Predicting the hydrogen storage capacity of alumina pillared interlayer clays using interpretable ensemble machine learning. *Int. J. Hydrogen Energy* **2025**, *120*, 354–364.
94. David, A.B.; Olalusi, O.B.; Awoyera, P.O.; et al. Suitability of Mechanics-Based and Optimized Machine Learning-Based Models in the Shear Strength Prediction of Slender Beams without Stirrups. *Buildings* **2024**, *14*, 3946.
95. Kyriakides, G.; Margaritis, K.G. *Hands-On Ensemble Learning with Python: Build Highly Optimized Ensemble Machine Learning Models Using Scikit-Learn and Keras*; Packt Publishing Ltd.: Birmingham, UK, 2019.
96. Lundberg, S.M.; Lee, S.I. A unified approach to interpreting model predictions. *Adv. Neural Inf. Process. Syst.* **2017**, *30*.
97. Wakjira, T.G.; Alam, M.S. Peak and ultimate stress-strain model of confined ultra-high-performance concrete (UHPC) using hybrid machine learning model with conditional tabular generative adversarial network. *Appl. Soft Comput.* **2024**, *154*, 111353.
98. Cao, Y.; Su, F.; Antwi-Afari, M.F.; et al. Enhancing mix proportion design of low carbon concrete for shield segment using a combination of Bayesian optimization-NGBoost and NSGA-III algorithm. *J. Clean. Prod.* **2024**, *465*, 142746.
99. Genç, B.; Tunç, H. Optimal training and test sets design for machine learning. *Turk. J. Electr. Eng. Comput. Sci.* **2019**, *27*, 1534–1545.
100. Akiba, T.; Sano, S.; Yanase, T.; et al. Optuna: A next-generation hyperparameter optimization framework. In Proceedings of the 25th ACM SIGKDD International Conference on Knowledge Discovery & Data Mining, Anchorage, AK, USA, 4–8 August 2019; pp. 2623–2631.
101. Dietterich, T.G. Approximate statistical tests for comparing supervised classification learning algorithms. *Neural Comput.* **1998**, *10*, 1895–1923.
102. Xiong, F.; Yang, W.; Zhang, Y.; et al. Study on the electromagnetic field aligning steel fibres in UHPC reinforced beams. *Cem. Concr. Compos.* **2023**, *143*, 105251.
103. Liu, Y.; Xie, J.; Yan, J. Flexural and fracture performance of UHPC exposed to low-temperature environment. *Constr. Build. Mater.* **2023**, *373*, 130865.
104. Guo, Y.; Wang, J. Experimental study on UHPC beams without web reinforcement under four-point bending: shear behaviour and size effect. *Constr. Build. Mater.* **2023**, *409*, 133802.
105. Yan, W.; Zhang, R.; Subedi, S.; et al. Experimental investigation on flexural performance of UHPC beams reinforced with steel-FRP bars. *Arch. Civ. Mech. Eng.* **2024**, *24*, 132.
106. Du, L.; Wu, D.; Wang, J.; et al. Experimental Study on Flexural Behavior of Retard-Bonded Prestressed UHPC Beams with Different Reinforcement Ratios. *Buildings* **2025**, *15*, 887.
107. Tian, X.; Fang, Z.; Liu, S.; et al. Monotonic flexural behaviour of steel-fibre reinforced UHPC beams at sub-zero temperatures. *Cem. Concr. Compos.* **2024**, *150*, 105550.
108. Wang, Z.; Liang, X.; Wan, S.; et al. Flexural behaviour and damage evolution of steel-reinforced UHPC beams at low temperatures. *Eng. Fail. Anal.* **2025**, *181*, 109925.
109. Yang, J.; Yan, K.; Doh, J.; et al. Experimental study on shear performance of UHPC beams at elevated temperatures. *Eng. Struct.* **2023**, *291*, 116304.
110. Jin, L.; Xie, C.; Yu, W.; et al. Shear failures and bearing capacity analysis of UHPC beams at low temperatures: Experiment and formulation. *Eng. Struct.* **2025**, *330*, 119903.
111. Ge, W.; Chen, Z.; Zhang, Z.; et al. Shear behavior of externally prestressed UHPC beams without stirrups. *Case Stud. Constr. Mater.* **2023**, *18*, e01766.